NASA/CR-2001-210662
ICASE Report No. 2001-4

Lagrangian Approach to Jet Mixing and Optimization of the Reactor for Production of Carbon Nanotubes

Alex Povitsky and Manuel D. Salas
ICASE, Hampton, Virginia

ICASE
NASA Langley Research Center
Hampton, Virginia

Operated by Universities Space Research Association

National Aeronautics and
Space Administration

Langley Research Center
Hampton, Virginia 23681-2199

Prepared for Langley Research Center
under Contract NAS1-97046

February 2001

LAGRANGIAN APPROACH TO JET MIXING AND OPTIMIZATION OF THE REACTOR FOR PRODUCTION OF CARBON NANOTUBES*

ALEX POVITSKY† AND MANUEL D. SALAS‡

Abstract. This study was motivated by an attempt to optimize the High Pressure carbon oxide (HiPco) process for the production of carbon nanotubes from gaseous carbon oxide. The goal is to achieve rapid and uniform heating of catalyst particles by an optimal arrangement of jets. A mixed Eulerian and Lagrangian approach is implemented to track the temperature of catalyst particles along their trajectories as a function of time. The FLUENT CFD software with second-order upwind approximation of convective terms and an algebraic multigrid-based solver is used. The poor performance of the original reactor configuration is explained in terms of features of particle trajectories. The trajectories most exposed to the hot jets appear to be the most problematic for heating because they either bend towards the cold jet interior or rotate upwind of the mixing zone. To reduce undesirable slow and/or oscillatory heating of catalyst particles, a reactor configuration with three central jets is proposed and the optimal location of the central and peripheral nozzles is determined.

Key words. jet mixing, Lagrangian approach, path lines, FLUENT, nanotechnology, carbon nanotubes

Subject classification. Fluid Mechanics

1. Introduction. This study is aimed at improving the performance of the High Pressure carbon oxide (HiPco) process used for production of carbon nanotubes from gaseous carbon oxide [12]. In the HiPco process, the catalyst particles $Fe(CO)_5$ initialize formation of carbon nanotubes from carbon oxide. The catalyst particles enter the HiPco reactor at room temperature and are heated up to 1000^oC in the reactor. To avoid formation of Fe clusters, which do not act as a good catalysts, the catalyst particles should be heated as quickly as possible. In the current reactor design, hot peripheral jets are used to heat the cold central jet that carries the catalyst particles (see Fig. 1).

The gas in the central jet and peripheral jets is high-pressure CO.

The goal of this study is to increase the mixing rate between jets in such a way as to maximize the heating rate of catalyst particles.

Usually, in chemical engineering and in energy technology the rate of mixing is estimated as a function of a spatial coordinate, for example, as the completeness of mixing in cross-sections along the reactor axis. According to Holdeman et al. [10], an optimum is generally used to identify flow and geometric conditions which lead to a uniform temperature distribution in a minimum downstream distance from the section of jet-injection. To achieve this optimum, the system of Navier-Stokes equations together with an appropriate model of turbulence are solved using an Eulerian approach [11, 6, 7]. This approach was used by the first author's preliminary study [14] to show that for fast jet mixing a high angle of incidence between jets is advantageous. However, a short spatial scale does not necessarily imply rapid and monotonic heating of the catalyst particles in temporal scale.

Three types of particle trajectories will be discussed in the current study (Fig. 2).

*This research was supported by the National Aeronautics and Space Administration under NASA Contract No. NAS1-97046 while the authors were in residence at ICASE, NASA Langley Research Center, Hampton, VA 23681-2199.

†Senior Staff Scientist, ICASE, NASA Langley Research Center, Hampton, VA 23681-2199 (e-mail: aeralpo@icase.edu).

‡Director, ICASE, NASA Langley Research Center, Hampton, VA 23681-2199 (e-mail: salas@icase.edu).

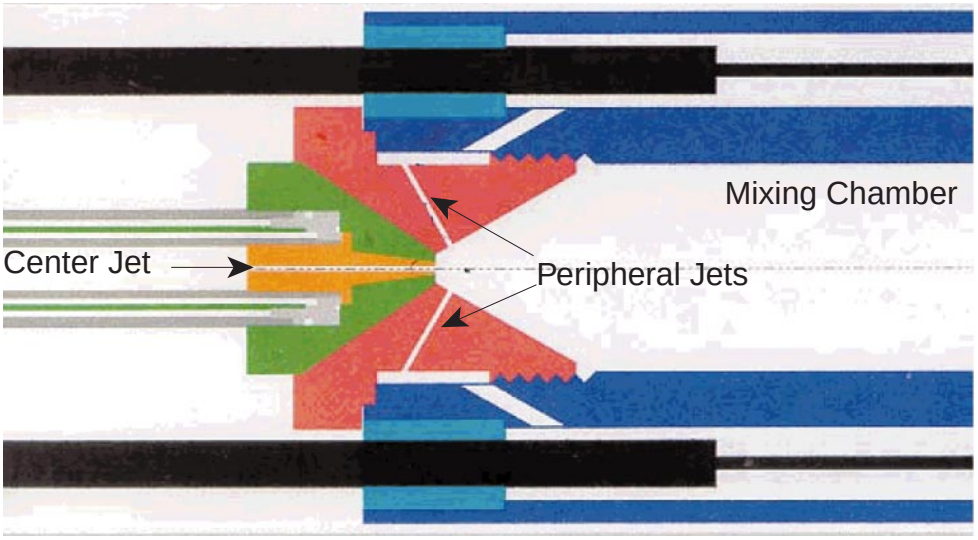

FIG. 1. *HiPco reactor. The cold central jet issues through the bottom, hot peripheral jets issue through side walls and meet at the centerline.*

Trajectory (1) bends inwards in the central jet, trajectory (2) is a representative of trajectories that bend outward, and trajectory (3) belongs to trajectories involved in the vortex formed upstream of the intersection of the jets.

It is shown here that at the high angle of incidence between mixing jets, the particle trajectories may either be bent substantially towards the cold jet interior or recirculate upstream of the jet intersection. This leads to a dramatic reduction of heating rate and to large oscillations of particle temperature. The computation of particle trajectories (also known as the Lagrangian approach) provides the explicit temporal evolution of the particle temperature. In this study, the computed temporal temperature profiles of the catalyst particles are used to find the optimal configuration of mixing jets.

The bending and rotation of trajectories, especially those that are mostly exposed to the hot jets and are therefore supposed to heat-up well cannot be avoided by simple procedures such as increasing the hot-to-cold jet mass ratio, increasing the angle between jets, and splitting the cold jet.

A special configuration of cold and hot jets which avoids direct exposure of the cold jet and provides roughly three times larger heating rate than the basic design is proposed and modeled here.

In Section 2, the design of the HiPCo reactor and its operation is described. In Section 3, the adopted mathematical model, implemented numerical methods, and the grid generation features are discussed in terms of the capabilities of the FLUENT CFD software [1] used in this study. In Section 4, the results of the reactor modeling are discussed. In Section 5, a novel configuration of nozzles is proposed and the results of modeling are compared with those for the basic reactor.

2. Description of the HiPco Reactor. The cold jet issues into the reactor working space through the central nozzle with $r_0 = .5$mm nozzle radius. The cone/cylinder working space of the reactor includes co-axial funnel ($L_f = 36r_0$, $R_1 = 4.35r_0, R_2 = 21.25r_0$) and cylindrical parts ($L_c = 75r_0, R = R_2$) (Fig. 3).

A smaller cylinder ($R = R_1, L_{c2} = 5r_0$) is co-axial with the funnel and surrounds the central nozzle (see Fig. 4).

The center of the smaller basis of the funnel is located at the origin (Fig. 4).

The central jet exit is located on the centerline ($z = 1.3$mm). The cold jet has a temperature of 373^o K

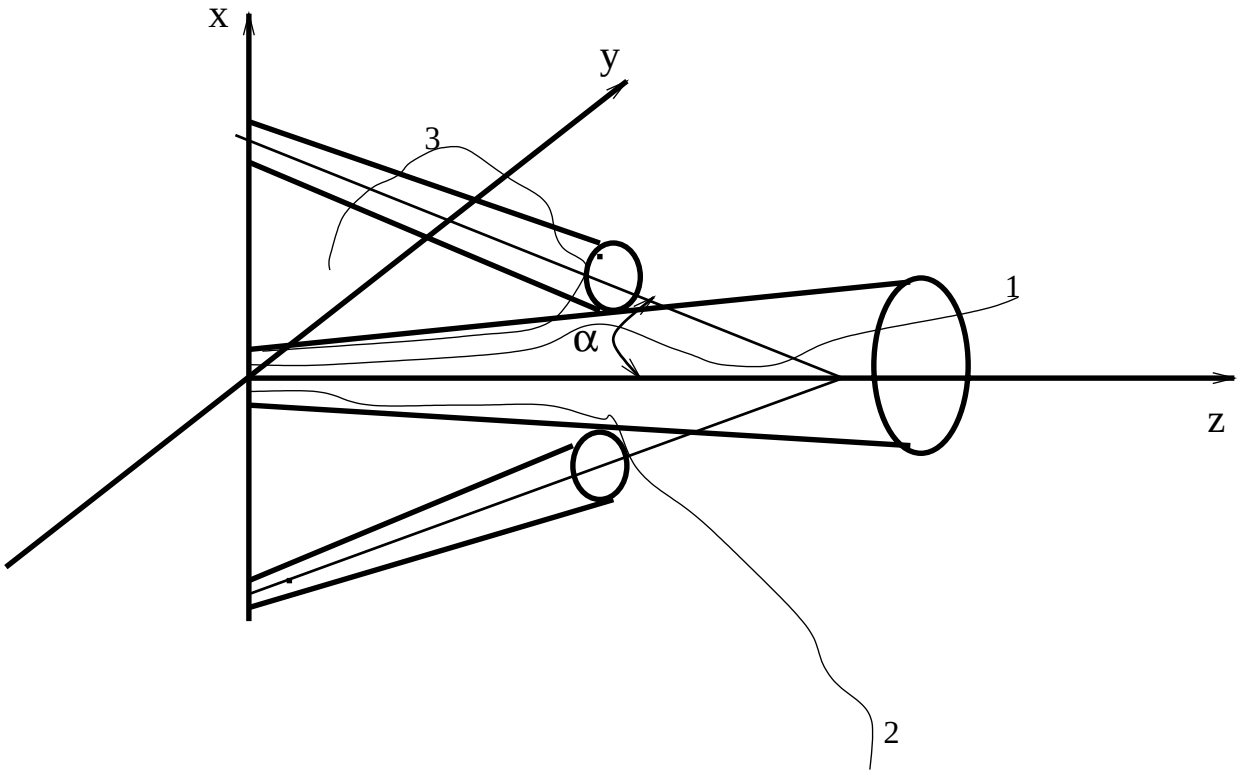

FIG. 2. *Behavior of trajectories for high-incidence jet mixing: (1) the trajectory bends inwards; (2) the trajectory bends outwards; and (3) the rotating trajectory.*

and a flow velocity of 37 m/s. Each hot jet exits through a peripheral nozzle with a 1.5 mm nozzle diameter after being heated to 1323^o K. For a $1:3$ mass ratio of central to peripheral jets, the peripheral jet velocity is 59 m/s. The reactor wall is heated to 1373^o K.

The centers of the peripheral nozzles (with radius $r_p = 1.5r_0$) are located at the reactor funnel ($z = 1$ mm, local funnel radius $R_p = 2.65$ mm) (Fig. 4). The jets are oriented so that the central and peripheral jets intersect at a point located at the reactor centerline. If the angle between the cold and peripheral jets is 30^0, this intersection point is located at distance 3.1 mm from the central jet exit and 4.3 mm from a peripheral jet exit.

To model the flowfield, the three-dimensional, steady Navier-Stokes equations are combined with an RNG $k-\epsilon$ turbulence model [16, 15]. Gas density and compressibility are described by the ideal gas model. Since jets intersect within $3-4$ diameters from their exits, their centerline velocity is equal to the jets' initial velocity. Note that at such a distance from the jet nozzle, the cross-sectional velocity profile is neither uniform nor self-similar [3]. The momentum flux ratio, $(\rho u^2)_c/(\rho u^2)_p$, where indices c and p denote central and peripheral jets respectively, is equal to 1.39, i.e., close to unity. Also, the cross-sections of the jets are of the same order of magnitude and none of the jets can be approximated by a uniform and infinitely wide cross-flow.

The Reynolds number based on the radius of the central jet nozzle is ≈ 1000, while the Reynolds number of the peripheral jet is ≈ 2000. Nevertheless, the jets are likely to be non-laminar even for relatively low Reynolds number [3]. In the high-pressure reactor, the fluid after passing the compressor is highly disturbed. In addition, non-parallel interaction between jets leads to sustained turbulence. The advantage of the RNG

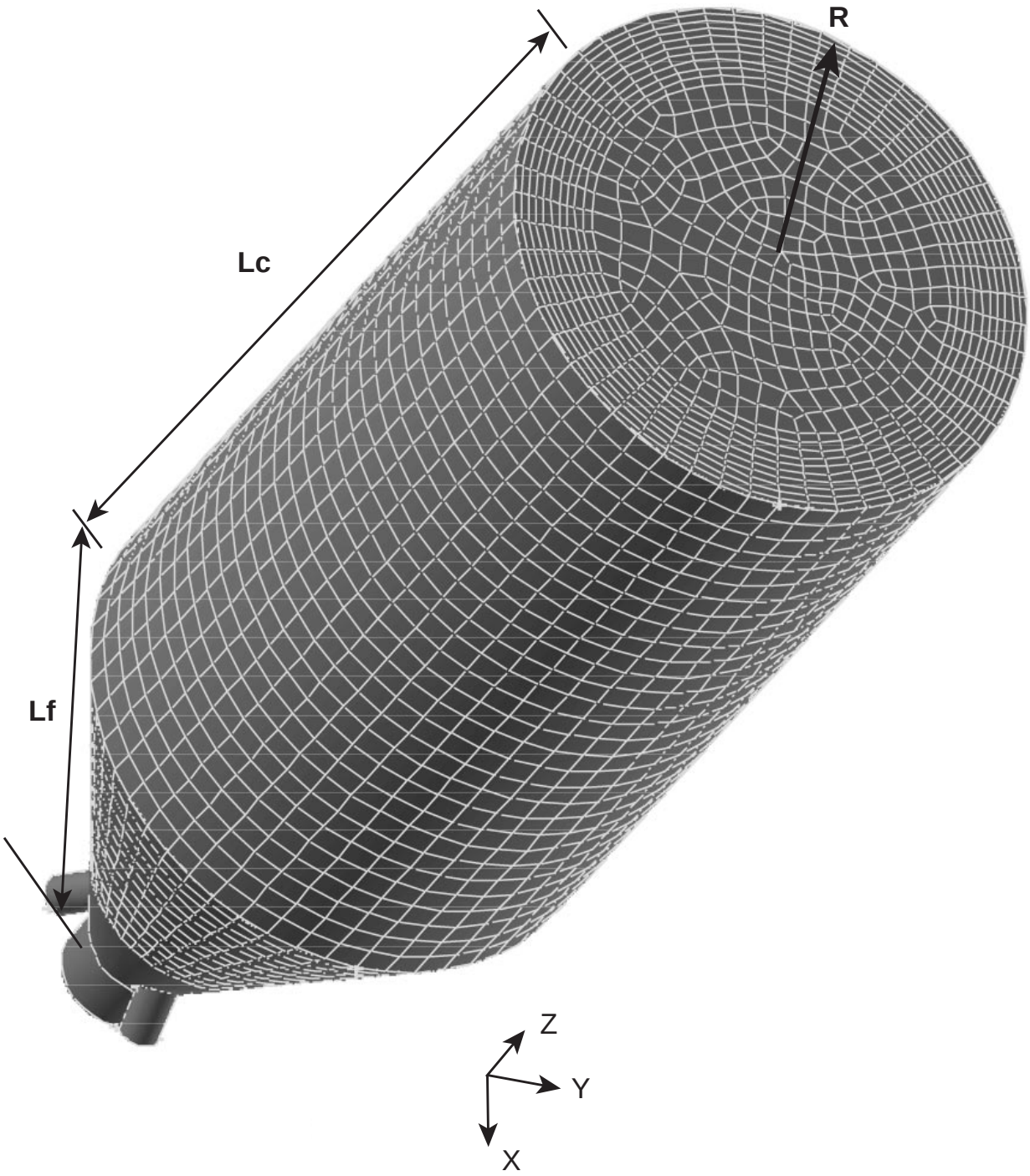

FIG. 3. *The computational volume and numerical grid.*

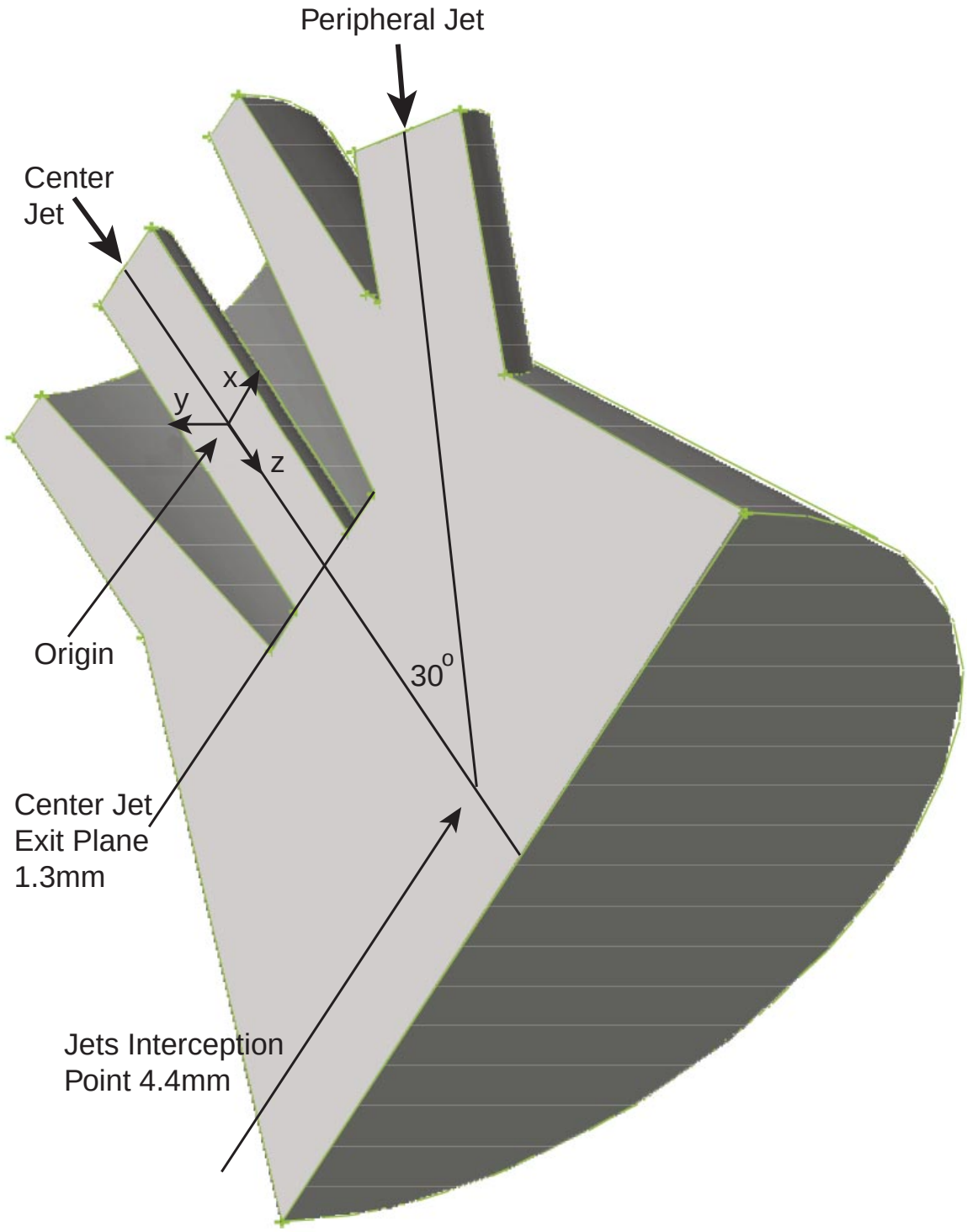

FIG. 4. *Showerhead of the reactor.*

$k-\epsilon$ model of turbulence, used in this study, is that it takes into account the low-Reynolds-number effects.

3. Numerical Method, Grid and Geometry Generation.

3.1. Computational volume and numerical grid generation. The computational volume and numerical grid are shown in Fig. 4.

To create the computational volume using the GAMBIT [2] package, the "top-down" approach is adopted, i.e., the geometry is constructed by creating volumes (bricks, cylinders, frustum, etc.), moving and rotating them, and then manipulating them through Boolean operations (unite, subtract, etc.). Thus, low-level operations such as creating vertices, edges, and faces are avoided.

Once the geometry is built, the numerical mesh is created by partitioning the entire domain onto sub-domains and then applying an appropriate meshing method to each of the sub-domains (Fig. 3). The most convenient Cooper scheme [4, 5] which is available in GAMBIT projects or extrudes a face mesh from one end of a volume to the other and then subdivides the extruded mesh to form the volume mesh. Unfortunately, the Cooper scheme is not valid for the showerhead geometry of two non-parallel cylindrical volumes. Therefore, the geometry should be decomposed into sub-domains in order to obtain sub-domains suitable for the Cooper tool. The reactor geometry is decomposed into two sub-domains (showerhead and cone/cylinder working space).

To mesh the cone/cylinder working space, the near-wall grid clustering, denoted as a grid boundary layer, is applied first. Grid boundary layers are layers of elements growing out from a boundary into the domain. In essence, the boundary layers are structured near-boundary pieces of grids incorporated into the overall grid. To improve the accuracy of the flowfield calculation and to provide an adequate grid for the solution of the RNG $k-\epsilon$ model of turbulence, this type of mesh is incorporated at the reactor wall. The grid cell hight closest to the wall is equal to $0.25r_0(\approx 0.0118R)$, the number of boundary layer grid nodes is 10, and the growing coefficient of the grid size is 1.02 (Fig. 3). The rest of this sub-domain is covered with hexahedral elements with $1r_0$ size using the Cooper algorithm. The axial section of the grid and the exit cross-section are shown in Fig. 3.

The showerhead (Fig. 4) is meshed by the Tet/Hybrid option of GAMBIT ($0.25r_0$ grid size) which composes the mesh primarily of tetrahedral mesh elements, but may include hexahedral, pyramidal, and wedge elements where appropriate.

3.2. Solution algorithm. The solution algorithm solves the governing equations sequentially. The directional momentum equations are each solved in turn using current values for pressure and cell face mass fluxes, in order to update the velocity field. Since the velocities obtained may not satisfy the continuity equation locally, a "Poisson-type" equation for the pressure correction is derived from the continuity equation and the linearized momentum equations [13]. This pressure correction equation is then solved to obtain the necessary corrections to the pressure and velocity fields and the face mass fluxes such that continuity is satisfied. Equations for scalars such as turbulence and radiation are solved using the previously updated values of the other variables.

FLUENT permits a choice of the discretization scheme for the convection terms of each governing equation. (Second-order accuracy is automatically used for the viscous terms.) For tetrahedral grids, since the flow is never aligned with the grid, the first-order convective discretization increases the numerical diffusion, and more accurate results can be obtained by using the second-order upwind discretization of convective terms [8]. However, the first-order discretization generally yields better convergence than the second-order scheme; therefore, in the current study computations start with the first-order scheme for all

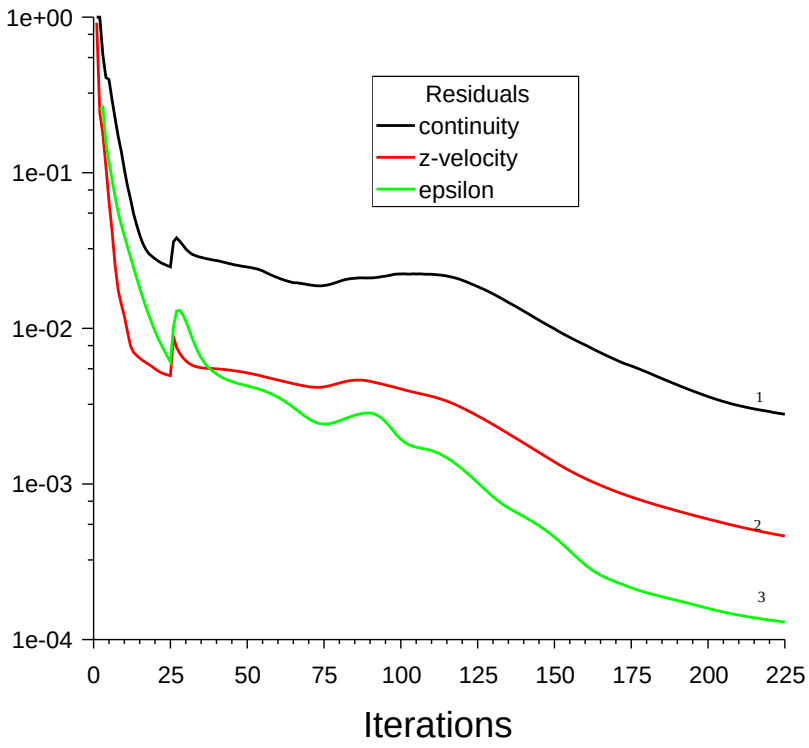

FIG. 5. *Convergence history: (1)-continuity, (2)-axial velocity, and (3)-dissipation of turbulent energy.*

equations and then switch to the second-order scheme (also for all equations) after some iterations.

FLUENT provides three methods for pressure-velocity coupling (see above) in the segregated solver: SIMPLE, SIMPLEC, and PISO. The Pressure-Implicit with Splitting of Operators (PISO) [9] pressure-velocity coupling scheme, part of the SIMPLE family of algorithms [13], is based on the higher degree of the approximate relation between the corrections for pressure and velocity. PISO with skewness correction is recommended for calculations on meshes with a high degree of distortion.

The Algebraic Multigrid (AMG) is used to solve linearized systems at each time step (iteration). This algorithm is referred to as an "algebraic" multigrid scheme because the coarse level equations are generated without the use of any geometry or re-discretization on the coarse levels; a feature that makes AMG particularly attractive for use on unstructured meshes.

The residual is the imbalance in a governing equation summed over all the computational cells. FLUENT scales the residual using a scaling factor representative of the flow rate of a variable through the domain.

The convergence in terms of the scaled residuals as the function of the number of iteration for continuity (curve 1), axial velocity (curve 2), and the dissipation of turbulent energy ϵ (curve 3) are presented in Fig. 5. The spike in the convergence curves at iteration 26 corresponds to the switch from the first-order approximation of convective terms to the second-order approximation with the PISO pressure-velocity coupling algorithm. The residuals are reduced three orders of magnitude for all variables before the iterations are completed.

In addition to solving transport equations for the continuous phase in the Eulerian framework, FLUENT has an option to simulate a discrete second phase in a Lagrangian frame of reference that includes the hydrodynamic drag and the discrete phase inertia. In our case, the inertia is negligible as the catalyst particles are of micron-size, therefore, the particle trajectories coincide with the flow path lines. Also, the particles temperature is equal to the local gas temperature.

4. Single Central Jet: Results and Discussion. First, computations were performed for a single central jet and three peripheral jets in the reactor described in Section 2 and denoted here as Design A. The angle between the central and a peripheral jets is taken equal to $30^o, 60^o$, and 90^o while the mass ratio (M) is taken equal to $1:3$ and $1:6$ (in the latter case the peripheral jet velocity is doubled). The cases are denoted as A30, A30-D, A60, A60-D, A90, and A90-D where the number after the letter "A" is the angle between the central and peripheral jets and the letter "D" means doubled hot gas consumption. For special cases of Design A where $\alpha = 90^o$, nozzles are located further downstream at the reactor funnel ($z = 3.1$ mm) to avoid interaction between peripheral jets and the internal cylinder surrounding the central jet nozzle.

The Design B of the reactor has a cylindrical workspace with the radius of cross-section equal to the entrance radius R_1 of the conical part of Design A. Design B has two opposite peripheral jets with the same exit radius r_p as for Design A.

The computed flowfield is presented in Figs. 6a,b for two limiting cases: $\alpha = 30^o, M = 1:3$ and $\alpha = 90^0, M = 1:6$, denoted as A30 and A90-D, respectively.

The velocity vectors are colored by the local flowfield temperature. The vectors are presented in the $x - z$ plane ($y = 0$). The centerline of the peripheral jet is located in this plane, so the interaction between the central and the peripheral jet in the plane of their centerlines is clearly seen in the left side of Figs. 6a,b. The right side of the plane in Figs. 6a,b is located between two other peripheral jets. In the Case A30, the peripheral jet merges with the central jet without the formation of a significant recirculation zone upstream of the intersection. On the contrary, the strong recirculation zone between the central and the peripheral jet is formed in the Case A90-D. Vortices are located aside of the jet centerlines and the low-speed stagnation zone appears upstream of the intersection of the jets near the central jet centerline. For the Case A90-D, the momentum flux ratio between the central and a peripheral jet is equal to 0.35, the peripheral jet reaches the intersection point without the formation of stagnation zone at its centerline.

The material of the central jet spreads aside between the peripheral jets. In the Case A30 (Fig. 6a) most of the flow vectors in the spreading region are directed in the z direction whereas in the Case A90-D the flow vectors are directed backward and form the recirculation zone near the reactor side wall.

The observed difference in jet interaction between the cases A30 and A90-D is caused by the fact that in the latter case the velocity component $|u|$ (normal to the central jet) is four times ($2/sin(30^o) = 4$) larger than that in the former case.

It is worthwhile to compare our results with the study [11] where the uniform cross-flow interacts with the row of jets issuing perpendicular to the cross-flow. The authors of [11] observed the formation of vortices downstream and upstream of the jet row which they call primary and secondary vortices, respectively. In our case, the upstream vortex is larger and stronger than the downstream vortex because of the cross-sectional non-uniformity of the central jet (as opposed to the uniform cross-flow). The peripheral part of the central jet has relatively low velocity and easily forms the vortex upstream of the peripheral jet, which can be viewed as a rigid obstacle. Also, the upstream vortex affects more the heating rate along the central jet path lines than the downstream vortex.

If the jet is strong enough, the cross-flow forms vortices around the jet rather than penetrating it.

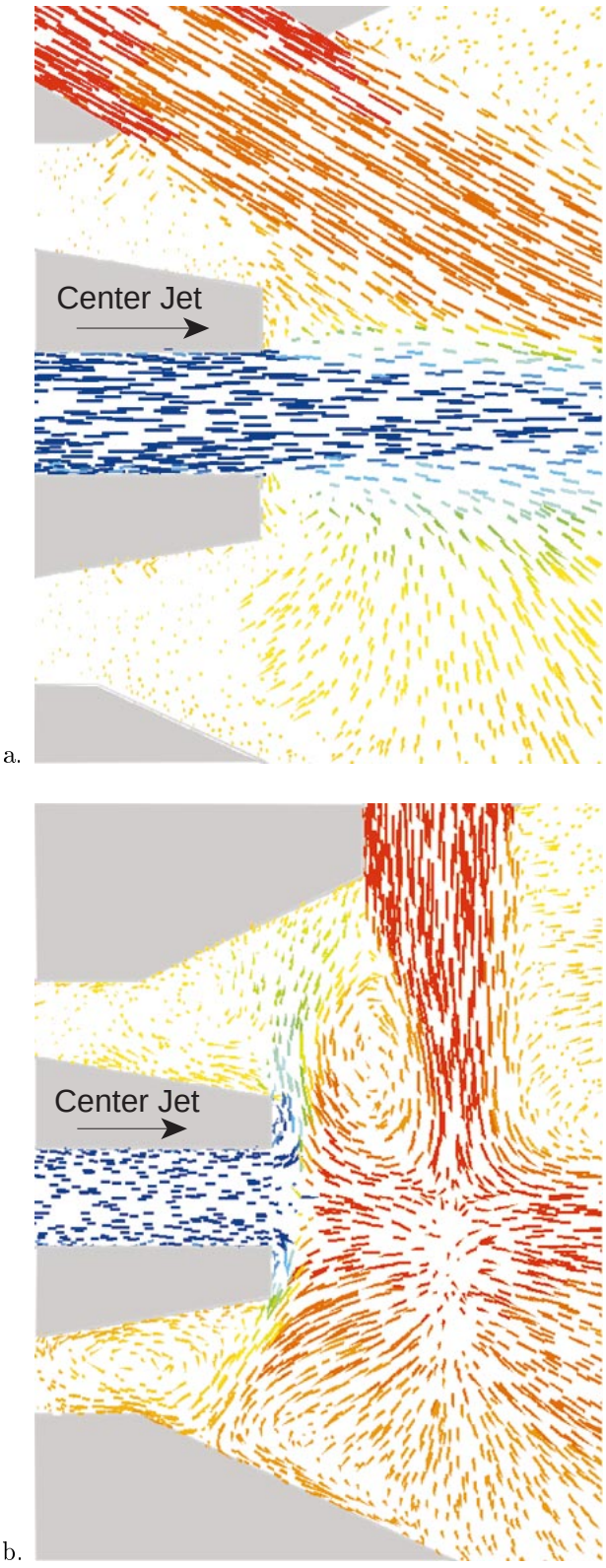

FIG. 6. *Flowfield in the $x-z$ section: a) $\alpha = 30^o, M = 1:3$; b) $\alpha = 90^o, M = 1:6$.*

When the jet strength weakens far downstream from its exit, the cross-flow is able to penetrate the jet and eventually split it [11]. In our case, the cross-sectional non-uniformity of the central jet and weakening of the peripheral jets (due to their counterflow type of interaction with each other) leads to a situation where the peripheral part of the central jet forms a vortex whereas the central part of this jet penetrates the peripheral jet. Both phenomena occur within approximately the same distance from the exit of the peripheral jet. This determines different mixing scenarios for various catalyst particles issuing uniformly from the central jet nozzle.

To study the temporal temperature profile, six path lines were chosen to represent catalyst particle trajectories. The initial radial distance from the center of the central nozzle is equal to $0.5r_0$ for the first three (inner) trajectories and $0.75r_0$ for the remaining (outer) trajectories. The angular coordinates in the nozzle cross-section $x-y$ are taken $\beta = 0, 30^o$, and 60^o. The first angular location is in the peripheral jet plane $x-z$, whereas the last location is exactly between two peripheral jets. Recall that the reactor is periodic in the cross-section with the angular span 120^o.

The temperature along the trajectories as a function of time for the cases A30, A30-D, A60, A60-D, A90, and A90-D is shown in Figs. 7a-f, respectively.

To get more insight into how the particles are heated, the distance from the reactor axis along particle trajectories $\sqrt{x^2+y^2}$ as a function of the axial coordinate z is plotted in Fig. 8a-f. The cases and the path lines are the same as in Fig. 7.

The cross-section corresponding to the peripheral nozzles and geometric intersection of the jets' axes are shown at the horizontal axis, symbols ! and x, respectively.

For $\alpha = 30^o$, the trajectories that are directly exposed to the core of the peripheral jet ($\beta = 0$) are inclined towards the centerline, i.e., they belong to the first category of trajectories (see Fig. 2). The remaining path lines are inclined outward, i.e. they fall into the second category of trajectories (see Fig. 2). The outer trajectories are bent higher and heated faster than the inner trajectories. The degree of bending primarily depends on the speed of the peripheral jets (compare the corresponding trajectories in Fig. 8a with Fig. 8b). The heating rate along the trajectories of the first type is the slowest, whereas the heating rate along the remaining trajectories increases with the initial radius and the initial angular position β.

Increasing the angle between jets up to $\alpha = 60^o$ leads to the bending of the trajectories considered towards the centerline (see Fig. 8c,d). In spite of the reduced spatial scale of the mixing zone, the temporal scale increases, i.e., the heating rate drops in comparison with the previous case. The only trajectory which is bending outwards has an initial position between the peripheral jets (Fig. 8d, curve 6). This trajectory has the best heating rate among all trajectories (Fig. 7d, curve 6). For both mass ratios, the 60^o angle between jets gives the worst performance in terms of the heating rate (slope of temporal temperature profile).

Further increase of the angle between jets up to $\alpha = 90^o$ changes the behavior of the trajectories so that those with initial positions between the peripheral jets are highly bent outwards (Fig. 7e, curves 5 and 6). For $M = 1:6$, some trajectories show closed loops, i.e., they fall into the third category. The 90^o angle between jets provides higher heating rate, however, strong temperature oscillations are observed.

Increasing the mass ratio up to $M = 1:12$ (Fig. 9a,b) bends some trajectories inwards whereas the rest of particles are involved in the rotating motion, (compare Fig. 9b with Figs. 8e and 8f). The temperature profiles along the trajectories show large oscillations.

Design B, which has 90^o angle of jet intersection, $M = 1:6$, and two strong peripheral jets, shows the worst scenario of particle heating. The slow heating along trajectories together with large temperature oscillations is caused by the rotational nature of the trajectories (see Figs. 9c,d).

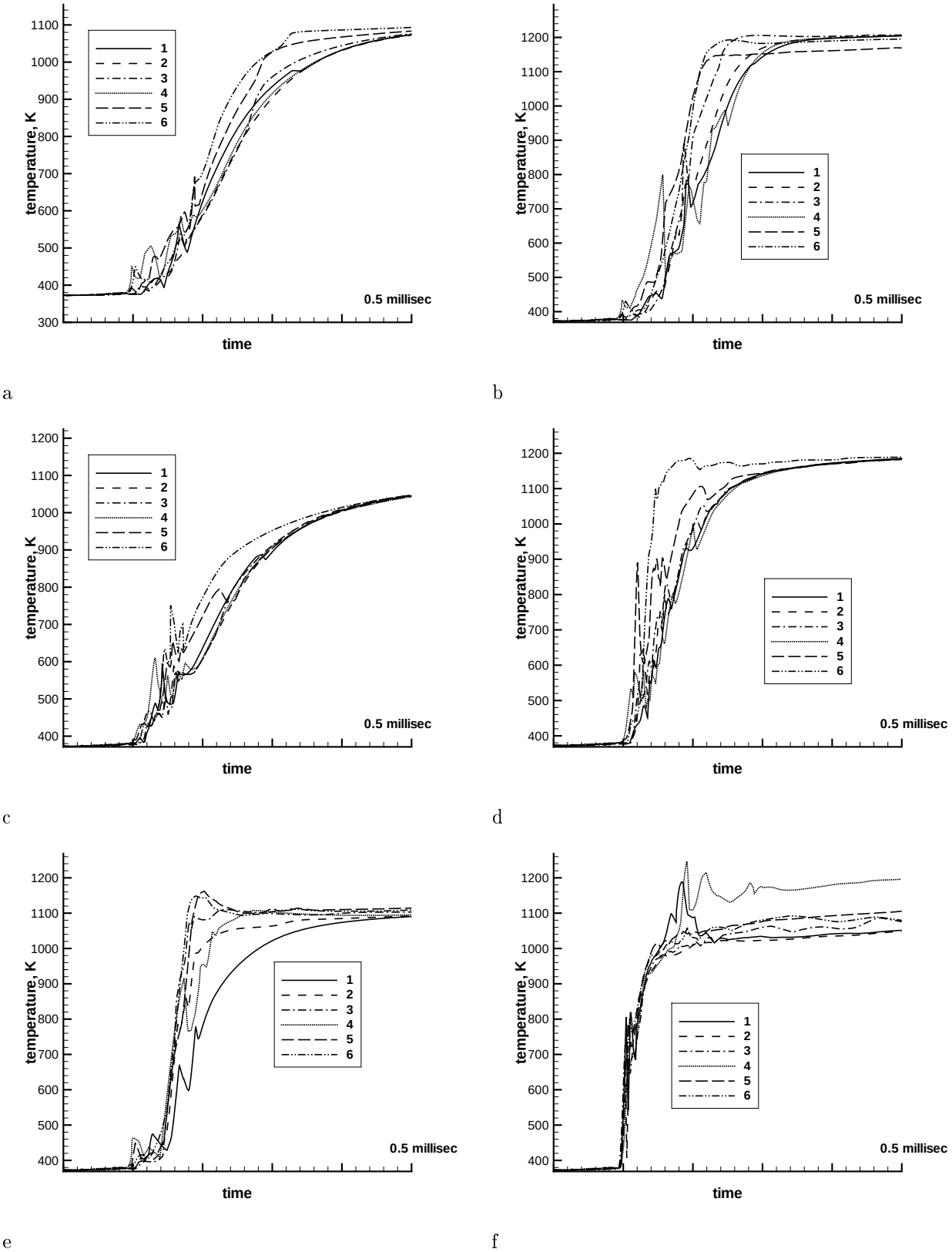

FIG. 7. *Temperature of catalyst particles. Angle α between the central and peripheral jets: a,b) $\alpha = 30^o$; c,d) $\alpha = 60^o$; and e,f) $\alpha = 90^o$. Mass ratio: a,c,e) 1 : 3; b,d,f) 1 : 6.*

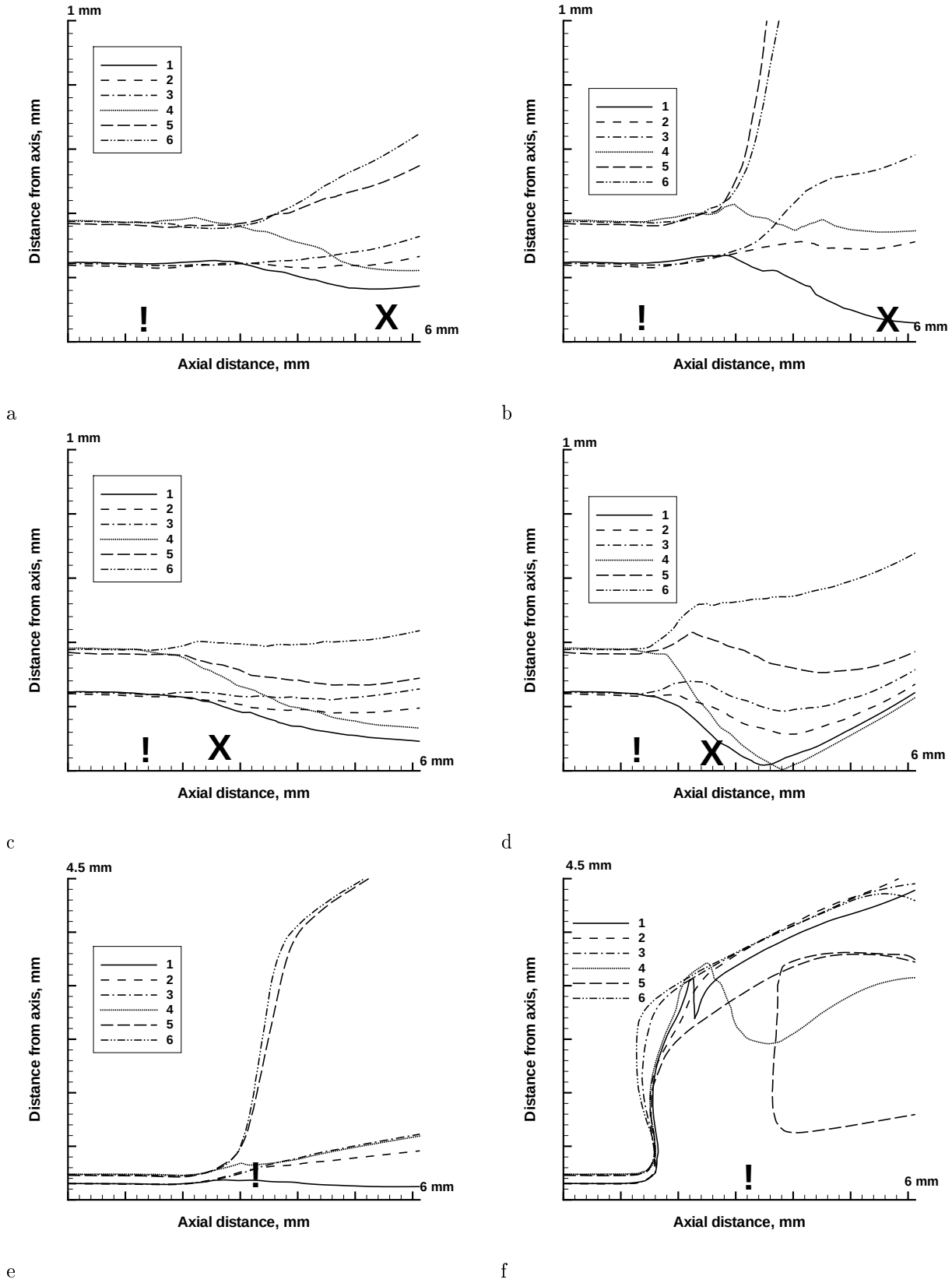

FIG. 8. *Trajectories of catalyst particles. Angle α between the central and peripheral jets: a,b) $\alpha = 30^o$; c,d) $\alpha = 60^o$; and e,f) $\alpha = 90^o$. Mass ratio: a,c,e) 1 : 3; b,d,f) 1 : 6. Symbols* X *and* ! *denote the geometric point of the jets' intersection at the reactor centerline and the cross-section with peripheral nozzles, respectively.*

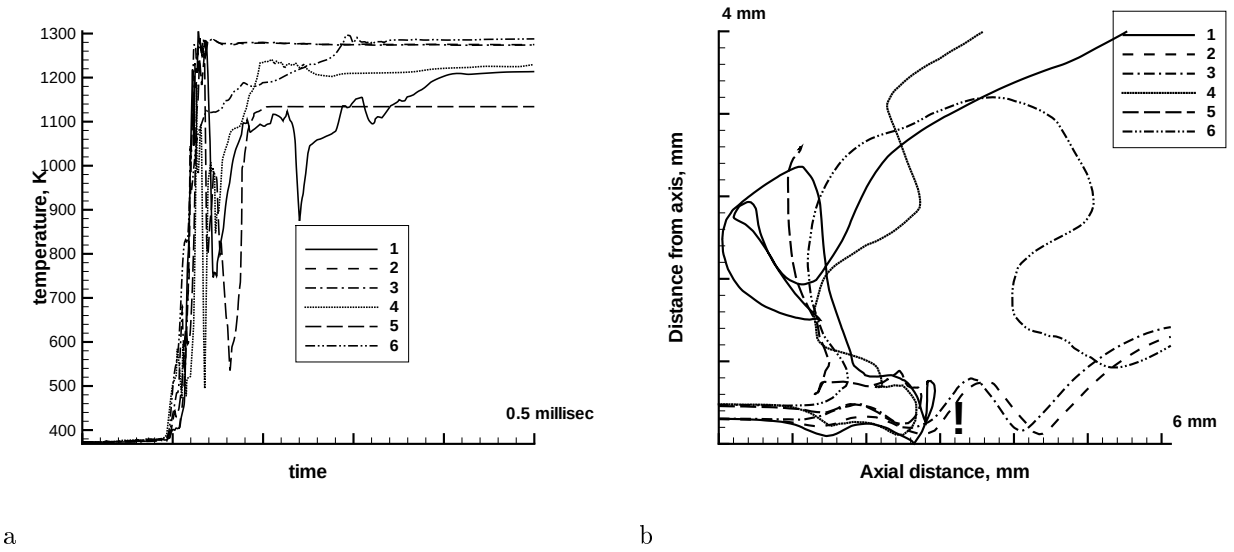

a b

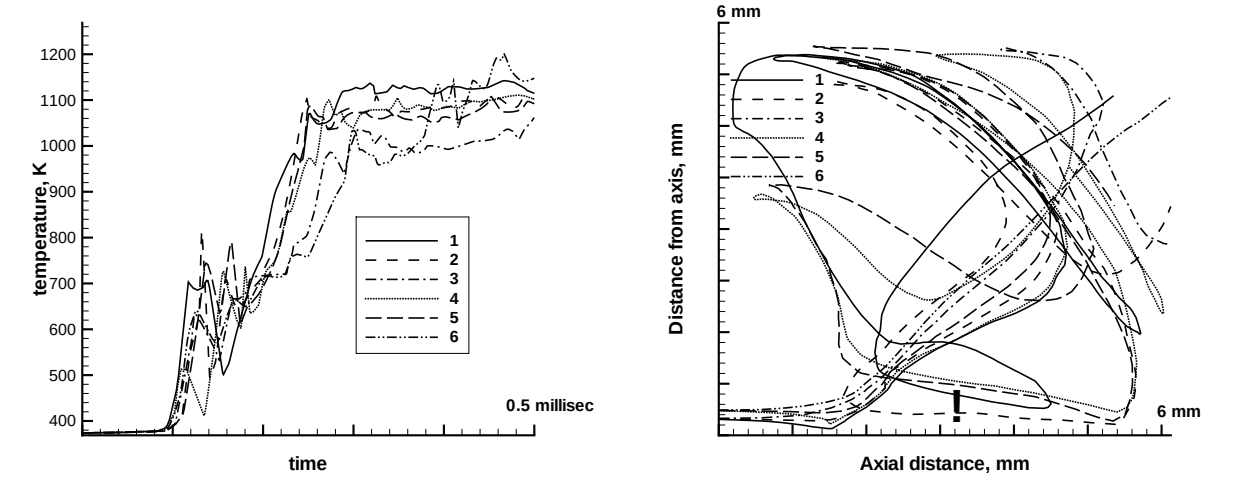

c d

FIG. 9. *Temperature and trajectories of catalyst particles for enhanced peripheral jet velocity: a-b) Mass ratio:* $1:12$; *and c-d) Reactor B, two peripheral jets, mass ratio* $1:6$.

The heating rate dT/dt (K/sec) at 800^oK as a function of the angle between jets for Design A is presented in Fig. 16b. The angle between the central and peripheral jets is taken as $30^o, 45^o, 60^o, 75^o$, and 90^o. Temperature profiles and coordinates of trajectories are presented in Figs. 7 and 8 for $30^o, 60^o$, and 90^o. The local minimum at 60^o corresponds to the case where trajectories belong to the first category (see Figs. 7b and 8b). At $\alpha = 45^o$, the trajectories are qualitatively similar to those at 30^o (Fig. 8a), however, they are more bent outwards and the heating rate reaches a local maximum. For the angles higher than 60^o, the heating rate strongly increases, however, the temperature profiles are oscillatory. For instance, two of six temperature curves cross the line 800^oK more than once at 75^o and four curves do so at 90^o. The heating rate becomes a multi-valued function of temperature for some trajectories; only the maximum value of heating rate is presented in Fig. 16.

To summarize, the goal of increasing the heating rate while avoiding temperature oscillations cannot be achieved by straightforward measures like increasing hot gas consumption or increasing the angle between hot and cold incident jets. The reason for this is the behavior of path lines. Inward-bending path lines (category one) show slow heating while rotating path lines (category three) have highly oscillating temperature profiles. Although the high angle between mixing jets leads to very short-scale spatial mixing, the heating of catalyst particles is relatively slow and the temperature oscillates along the particle trajectories.

5. Reactor with Three Central Jets. To increase the heating rate along trajectories, a modified reactor design was proposed which includes three parallel nozzles for cold central jets. Two variants of this design are denoted as Design C and Design D (see below).

The radius of the central nozzles is chosen to keep the same overall cross-sectional surface as that for the single central nozzle, i.e. $r_c = r_o/\sqrt{3}$. The centers of the central nozzles are located at a distance $2r_c$ from the reactor centerline and form an equilateral triangle. The peripheral jets are arranged as in the basic Design A.

In Design C, a plane containing the reactor centerline and a central jet nozzle makes an angle of 60^o with the peripheral jet nozzle planes (Fig. 10a). In Design D, central jet nozzles and corresponding peripheral jet nozzles are in the same plane.

Design D represents a straightforward split of the single central jet into three straight central jets and is examined first. The three jets are equivalent; therefore, the six trajectories are chosen to issue from the same jet. As in the previous cases, initial radial distance from the center of the central nozzle is taken equal to $0.5r_c$ for the first three trajectories and $0.75r_c$ for the remaining trajectories. The angular coordinates are taken as $\beta = 0, 90^o, 180^0$ and 270^o. Results for $\alpha = 30^o$ are presented in Fig. 11a,b. Unfortunately, the heating rate is worse than for the single central jet (compare Fig. 11a with Fig. 7a).

The reason for the slow heating is that all trajectories are bent towards the reactor centerline (Fig. 11b). Therefore, the straightforward split of the central jet does not help to achieve high heating rate.

To avoid direct exposure of the trajectories to the action of the hot jets, Design C is based on a rotation of the location of central and peripheral nozzles (see Figs. 10a and 12).

To show the most critical trajectories, the initial and final cross-sections of peripheral jets and central jets are presented in Fig. 12. The initial positions of the three peripheral jets (projection on a cross-section $x - y$) are shown as ellipses and denoted as $1, 2$, and 3. The final position of one of the peripheral jets is shown as a dashed ellipse. The two initial angular positions of trajectories are chosen as $\beta = 0^o$ and 180^o. The former location is the closest to jet 1 while the latter location is the most peripheral. The choice of the initial location of the remaining couple of trajectories (closest to the jets 2 and 3) is not straightforward as far as the mutual location of central and peripheral jets in $x - y$ cross-sections is varied with the axial coordinate z. The angle β_1 corresponds to the exit of peripheral jet 2 while the angle β_2 corresponds to the approximate final location of the peripheral jet 2 before it merges with other peripheral jets. The angles β_1 and β_2 are calculated from corresponding triangles. The angle $\beta_{av} = 0.5(\beta_1 + \beta_2)$ is taken as an averaged angle between two limit positions. For the given reactor geometry, $\beta_1 = 108.1^o, \beta_2 = 72.9^o$, and $\beta_{av} = 90.5^o$.

The temperature profiles along trajectories with angular locations β_1, β_2, and β_{av} are similar to each other (see Fig. 13f, $\alpha = 60^o$.)

In Figs. 13, 14, and 15, the angle β_1 is chosen for the representative trajectory. For $\alpha \leq 60^o$ (Figs. 14a,b), the trajectories fall into the second category. The most bent trajectories have initial position $\beta = 180^o$ while trajectories with initial $\beta = 0^o$ remain least bent. As opposed to Design A, no first-type trajectories are observed (compare Figs. 14a,b with Figs. 8a,c, respectively). This is the major advantage of Design C

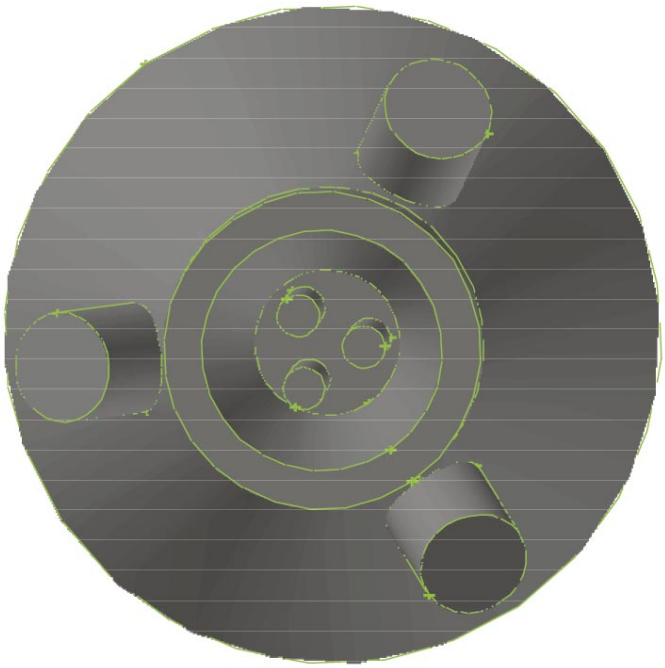

a.

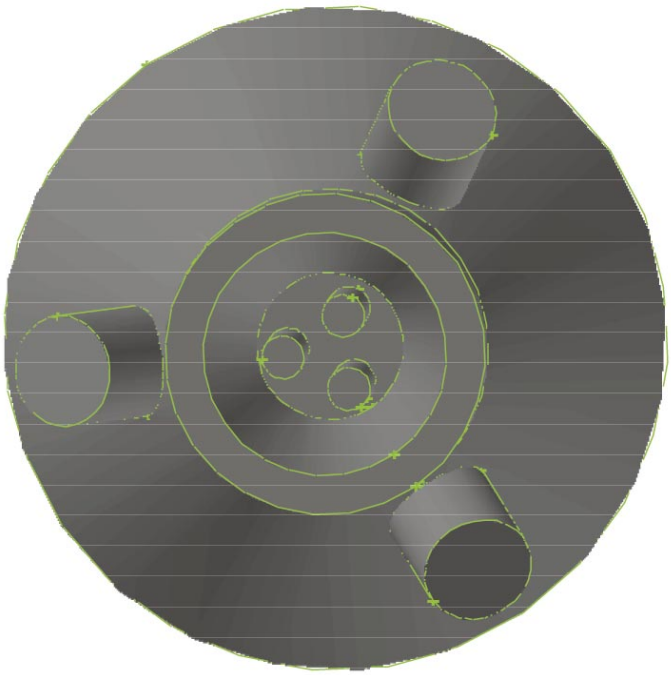

b.

FIG. 10. *Showerheads: a) Design C; and b) Design D.*

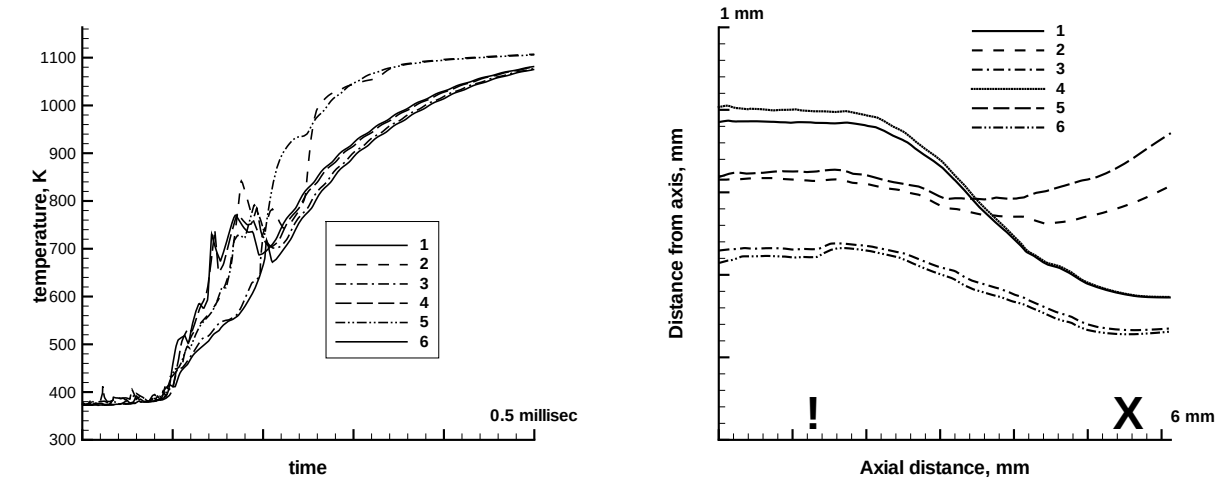

a b

FIG. 11. *Temperature and trajectories of catalyst particles for the case D3,* $\alpha = 30^0$.

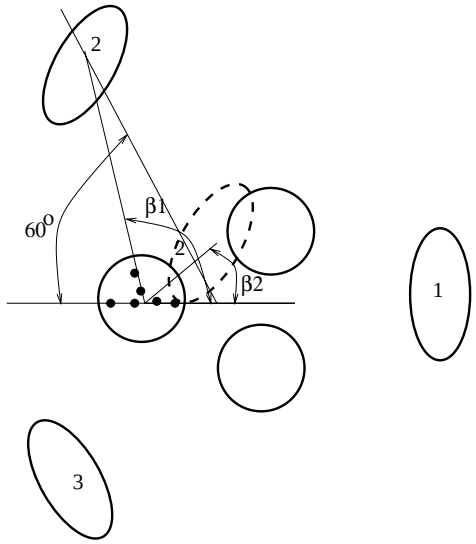

FIG. 12. *Initial coordinates of particles for Design C. Dashed ellipse denotes the approximate final cross-section of the peripheral jet. Symbols • denote initial positions of the considered trajectories.*

leading to considerably higher heating rate than that for Design A (compare Fig. 13a,b,c,f with Fig. 7a,c). For Design C, the optimal nozzle arrangement with $\alpha = 60^o$ provides a heating rate $3.5^o - 4.8^o \times 10^5 K/sec$ where $T = 800^o K$ (see Fig. 15). On the contrary, for Design A with its optimal $\alpha = 45^o$, the heating rate is in the range $1^o - 1.5^o \times 10^5 K/sec$.

Although further increase of the angle between jets to 75^o provides higher heating rate than that for 60^o (Fig. 16a), some trajectories appear to switch to the third type. For 90^o angle between jets, the trajectories become highly rotating (Fig. 14c) and temperature profiles strongly oscillate (Fig. 13e).

For Design C ($\alpha = 60^o$), the flowfield in the longitudinal section ($x - z$ plane) is presented in Fig. 17a. The velocity vectors of a cold central jet are directed outward and no significant longitudinal vortices are

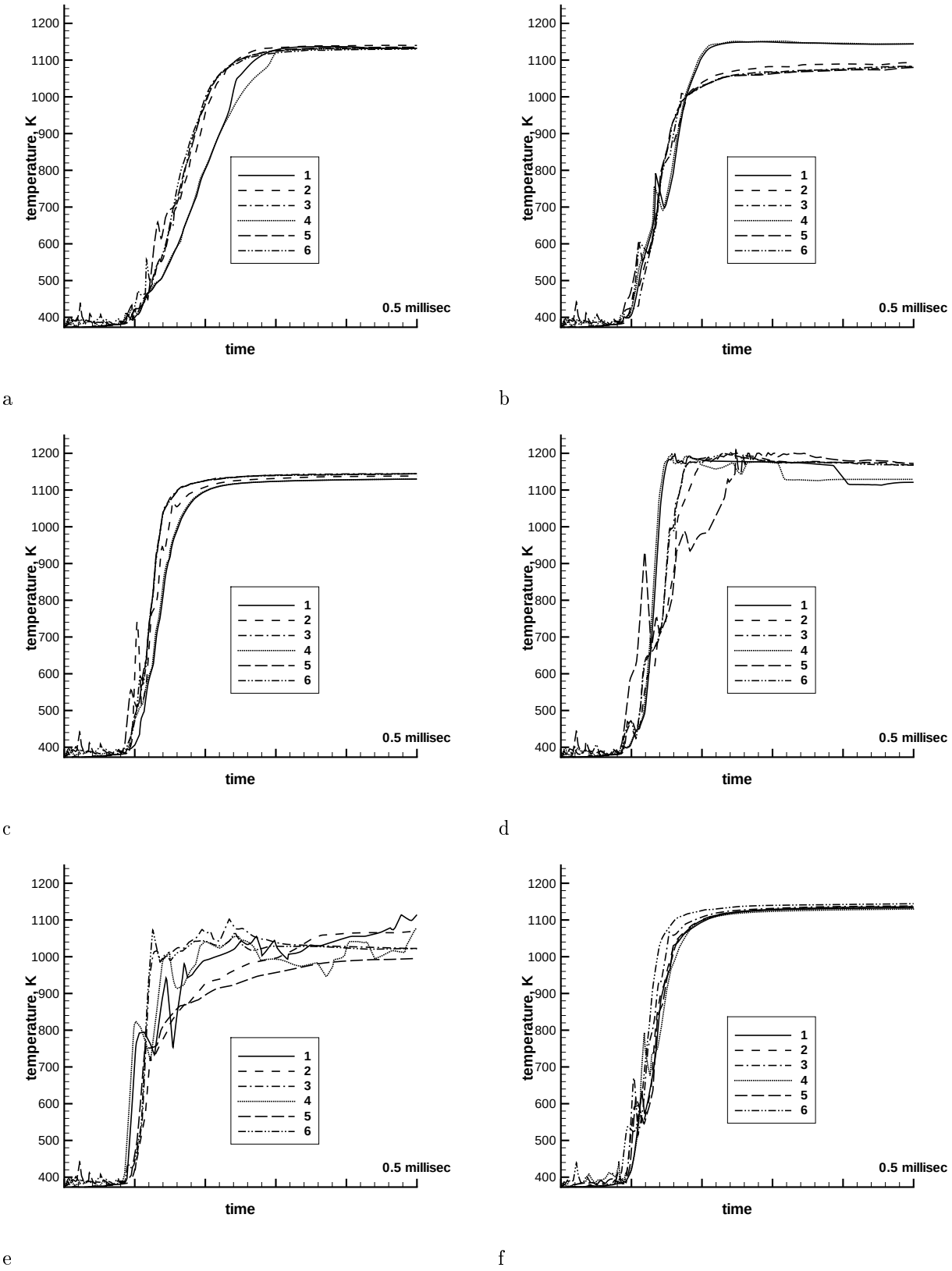

FIG. 13. *Temperature of catalyst particles for three central parallel jets. Angle α between the reactor axis and peripheral jets: a) $\alpha = 30^o$; b) $\alpha = 45^o$; c) $\alpha = 60^o$; d) $\alpha = 75^o$; e) $\alpha = 90^o$; and f) $\alpha = 60^o; \beta = \beta_1, \beta_2, \beta_{av}$.*

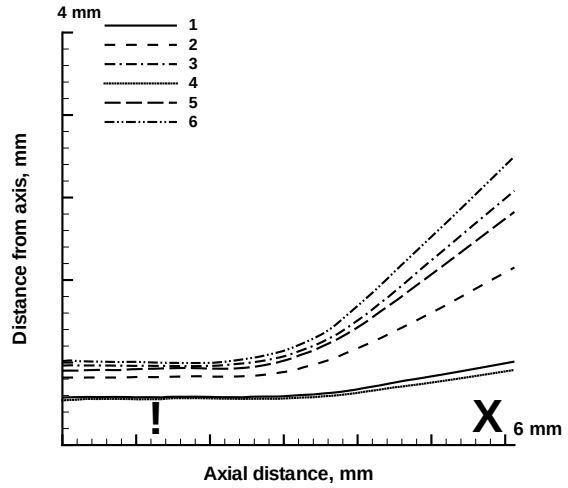

a.

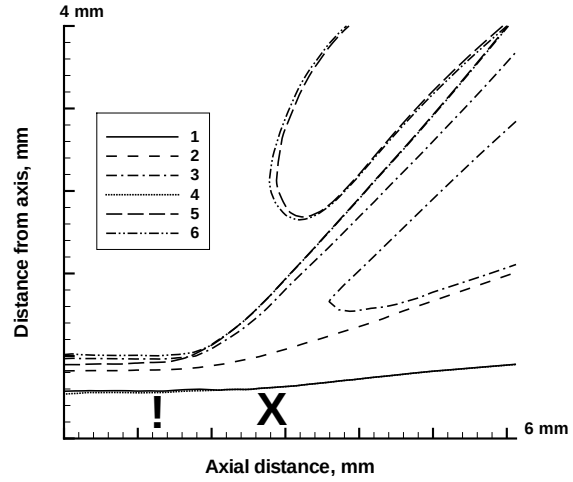

b.

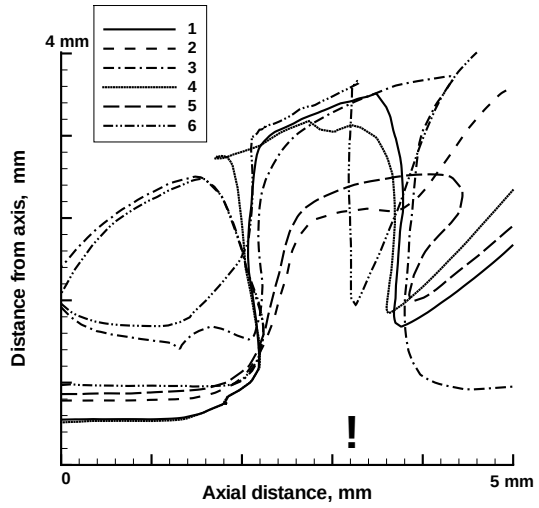

c.

FIG. 14. *Trajectories of catalyst particles for three central parallel jets. Angle α between the reactor axis and peripheral jets: a) $\alpha = 30^o$; b) $\alpha = 60^o$; and c) $\alpha = 90^o$.*

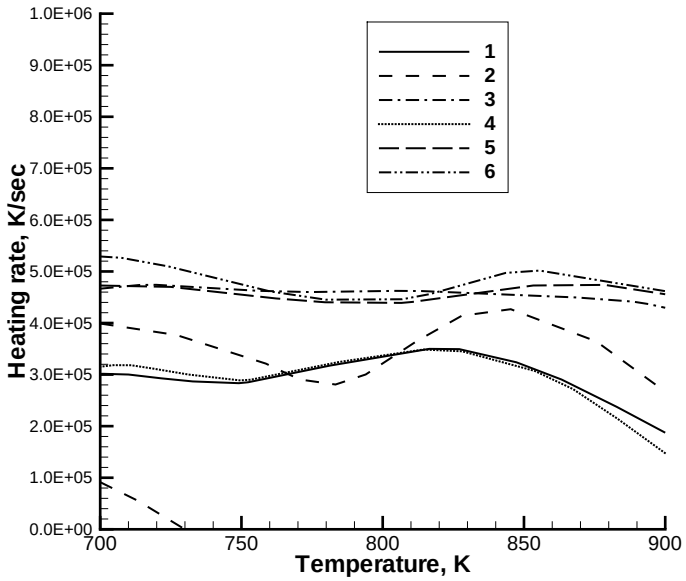

FIG. 15. *Heat rate of catalyst particles versus temperature for* $\alpha = 60^0$. *Temperature interval* $700 - 900K$ *is taken.*

observed. In fact, the visible peripheral jet, which corresponds to the jet 1 in Fig. 12, interacts with the visible central jet after the peripheral jets merge resulting in annihilation of their normal velocity components. In the cross-section with the z coordinate corresponding to the jets' intersection point (Fig. 17b), the material of the central jets is directed outwards between the peripheral jets. The vortices appear due to interaction of these outward-directed fluxes with the reactor wall. However, the particles have already been heated before they enter these vortices.

6. Conclusions. Jet mixing in a reactor for production of carbon nanotubes from gaseous carbon oxide initiated by catalyst particles is studied numerically using a mixed Eulerian and Lagrangian approach.

To achieve rapid monotonic heating of catalyst particles, the behavior of particle trajectories is studied. Three types of trajectories are observed. The particle trajectories can be bent either towards the interior of the cold jet (type 1), or outward (type 2). They also can rotate in the vortical zone upstream of the intersection of cold and hot jets (type 3). Direct exposure to the action of hot jets leads to the first or to the third type of trajectory behavior that causes slow or oscillating heating, respectively.

For the basic configuration of the reactor (one central and three peripheral jets), many trajectories are either of type 1 (for angle between jets $\alpha = 60^o$) or type 3 (for $\alpha > 60^o$). For smaller α, the type 2 trajectories provide steady, but slow heat-up. The optimal angle between jets, $\alpha = 45^o$, provides heating rate $1^o - 1.5^o \times 10^5 K/sec$ for most of the trajectories considered at $T = 800^o K$.

Straightforward measures such as increasing hot gas consumption, increasing the angle between hot and cold incident jets, and splitting the cold jet are not sufficient to achieve fast heating because of the behavior of particle trajectories.

A modified reactor design has been proposed, Design C, which includes three parallel nozzles for cold central jets. To avoid direct exposure of trajectories to the action of hot jets, the cold jet nozzles are located between the hot peripheral jet nozzles. Type 1 trajectories are avoided and at the optimal angle between

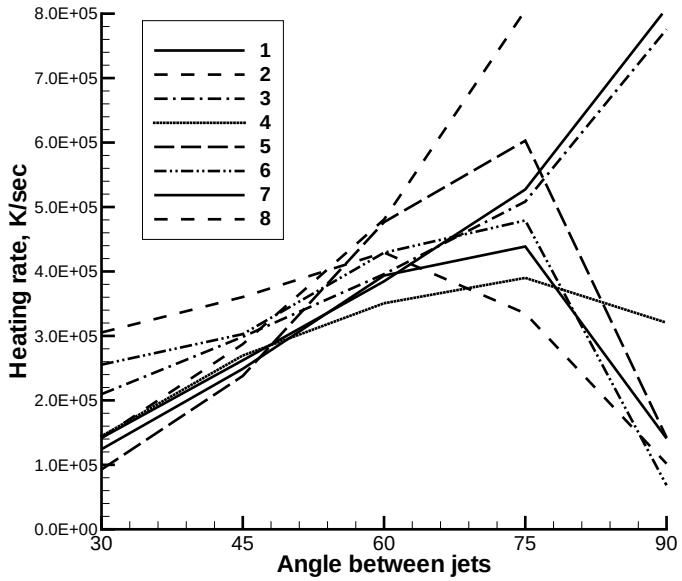

a.

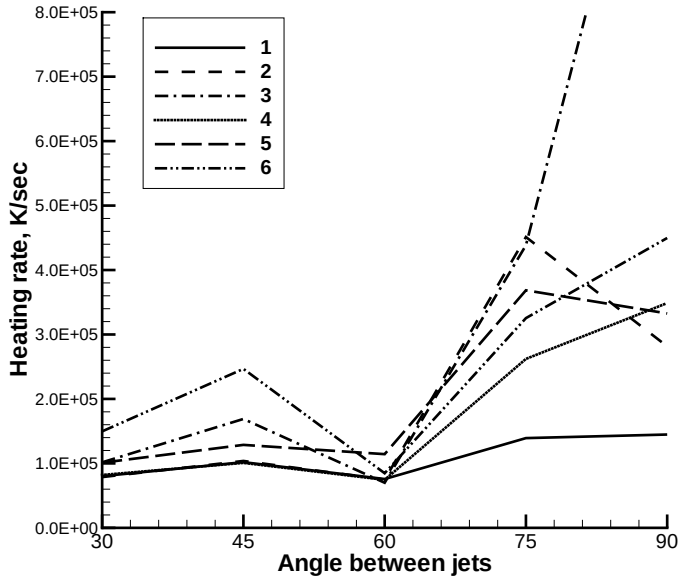

b.

FIG. 16. *Heat rate at* $800K$ *as a function of angle between jets: a) Design C; and b) Design A.*

jets, $\alpha = 60^o$, the heating rate reaches $3.5^o - 4.5^o \times 10^5 K/sec$, a significant improvement compared to the rate achieved by the basic design.

REFERENCES

[1] *FLUENT 5.0 User's Manual*, Fluent Inc., Lebanon, NH, 2000. http://www.fluent.com.

[2] *GAMBIT 1.2 User's Manual*, Fluent Inc., Lebanon, NH, 2000. http://www.fluent.com.

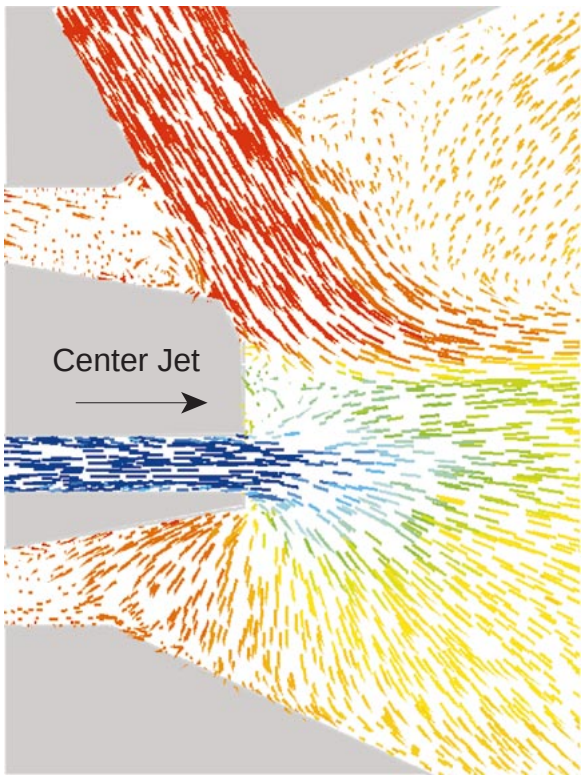

a.

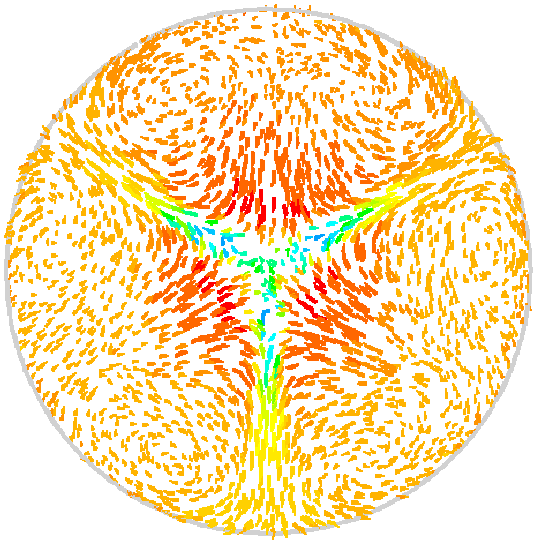

b.

FIG. 17. *Flowfield, Design D, $\alpha = 60^0$: a) $x - z$ plane, velocity vectors colored by the local temperature; b) $x - y$ cross-section at jet intersection point.*

[3] G. N. Abramovich, *The Theory of Turbulent Jets*, The MIT Press, Cambridge, MA, 1963.

[4] T. Blacker, *The Cooper Tool*, in Proceedings of the 6th International Meshing Roundtable Conference, Park City, UT, 1997. http://www.imr.sandia.gov/.

[5] T. Blacker and K. Miyoshi, *Hexahedral Mesh Generation Using Multi-axis Cooper Algorithm*, in Proceedings of the 9th International Meshing Roundtable Conference, New Orleans, LA, 2000. http://www.imr.sandia.gov/.

[6] J. P. Drummond, M. H. Carpenter, and D. W. Riggins, *Mixing and Mixing Enhancement in Supersonic Reacting Flowfields*, Progress in Asronautics and Aeronautics, 137 (1991), pp. 383–455.

[7] J. P. Drummond and P. Givi, *Suppression and enhancement of mixing in high-speed reacting flow fields*, in Combustion in High-Speed Flows, J. Buckmaster et al., ed., Kluwer Academic Publishers, Printed in the Netherlands, 1994, pp. 191–229.

[8] C. Hirsch, *Numerical Computation of Internal and External Flows, Vol. 1: Fundamentals of Numerical Discretizations*, John Wiley, Chichester, 1994.

[9] R. I. Issa, *Solution of Implicitly Discretized Fluid Flow Equations by Operator Splitting*, J. Comput. Phys., 62 (1986), pp. 40–65.

[10] J. D. Holderman et al., *Mixing of Multiple Jets With a Confined Subsonic Crossflow in a Cylindrical Duct*, NASA Technical Memorandum 107185, NASA Lewis Research Center, 1996. ASME-96-GT-482, Prepared for the 41st Gas Turbine and Aeroengine Congress, ASME, Birmingham, UK, June 1996.

[11] S.-W. Kim and T. J. Benson, *Fluid Flow of a Row of Jets in Crossflow - A Numerical Study*, AIAA Journal, 31 (1993), pp. 806–813.

[12] P. Nikolaev, M. Bronikowski, R. K. Bradley et al., *Gas-phase Catalytic Growth of Single-walled Carbon Nanotubes from Carbon Monoxide*, Chemical Physics Letters, 313 (1999), pp. 91–97.

[13] S. Patankar, *Numerical Heat Transfer and Fluid Flow*, Hemisphere Publishing Co., New York, 1980.

[14] A. Povitsky, *Improving Jet Reactor Configuration for Production of Carbon Nanotubes*, ICASE Report No. 2000-18, 2000. Submitted to *Computers and Fluids*.

[15] A. Yakhot, S. A. Orszag, V. Yakhot, and M. Israeli, *Renormalization Group Formulation of Large-eddy Simulation*, Journal of Scientific Computing, 4 (1989), pp. 139–158.

[16] V. Yakhot and S. A. Orszag, *Renormalization Group Analysis of Turbulence: I. Basic Theory*, Journal of Scientific Computing, 1 (1986), pp. 1–51.